ORIGINAL RESEARCH

Towards the simulation of mould filling with polymer composites reinforced with mineral fillers and short fibres

**Olivier Guiraud · Pierre J. J. Dumont ·
Laurent Orgéas · Jean-Pierre Vassal ·
Thai-Hung Le · Denis Favier**

Abstract Bulk Moulding Compounds (BMC's) are short fibre reinforced polymer composites that behave, during their forming, as concentrated fibre suspensions. Their suspending fluid is also a concentrated granular suspension made up of the polymer filled with mineral fillers. In this work, a method is proposed to model their flow. Firstly, the rheology of an industrial BMC was analysed by performing two types of mechanical tests, i.e. lubricated simple and plane strain compression experiments. Experimental results underline the roles of the current strain, the strain rate as well as the mechanical loading on the rheology of the BMC. Secondly, a 3D tensorial rheological model is proposed to reproduce the simple and plane strain compression experiments. Then this model is implemented into a Finite Element code dedicated to the simulation of compression moulding. Simulation results are finally compared with experiments achieved with rather complex flow situations.

Keywords Polymer composites · Fibre suspension · Granular system · Rheometry · Process simulation · Compression moulding · Bulk Moulding Compounds (BMC)

O. Guiraud · L. Orgéas (✉) · J.-P. Vassal ·
T.-H. Le · D. Favier
Laboratoire Sols-Solides-Structures-Risques (3SR),
CNRS / Université de Grenoble, BP 53 38041
Grenoble cedex 9, France
e-mail: Laurent.Orgeas@grenoble-inp.fr

P. J. J. Dumont
Laboratoire de Génie des Procédés Papetiers (LGP2),
CNRS / Institut Polytechnique de Grenoble
(Grenoble INP), 461 rue de la Papeterie,
BP 65, 38402 Saint-Martin-d'Hères cedex, France

T.-H. Le
Faculty of Material Science and Technology,
Hanoi University of Technology,
1 Dai Co Viet Road, Hanoi, Vietnam

Introduction

Bulk Moulding Compounds (BMC) are polymer composite materials. Their matrix is made up of $\approx$ 20–40 wt.% thermoset polymer (polyester) with a high content ($\approx$ 40–60 wt.%) of mineral fillers ($CaCO_3$, Al_2O_3). The matrix is reinforced by $\approx$ 20–30 wt.% of short entangled glass fibres. BMC's are widely used by the electric industry to produce small components with good surface quality and complex shapes, as well as by the automotive industry to produce for example car panels. Their processing consists in (i) the compounding phase, i.e. mixing uncured polyester resin, mineral fillers, glass-fibre bundles and other additives, (ii) the injection or compression moulding phase (1–10 s) during which these compounds are forced to fill a hot mould (150°C), (iii) the resin cure within the hot mould (60–180 s). During forming (stage (ii)), BMC's behave as concentrated fibre suspensions with a suspending fluid, which is also a concentrated granular suspension made up of a liquid polymer filled with a high content of mineral fillers.

Many studies in the literature deal with the experimental characterisation of the rheology of "standard" polymer composites reinforced by short, long or con-

tinuous fibres or fibre bundles, by subjecting these semi-dilute or concentrated fibre suspensions to shear, elongational, lubricated compression or squeeze flows (e.g. [3, 12, 17, 21, 23, 25, 46–48, 51, 54]). These studies were the basis to establish or validate rheological models that can be used to simulate the forming processes of these composites (e.g. [4, 16, 32, 33, 37, 49, 52, 56, 58]).

However, less is known on the rheology of fibre-reinforced polymer composites when the polymer is also filled with solid particles, i.e. when the suspending fluid is also a concentrated granular suspension [15]. For example, some studies were carried out to understand the rheology of Sheet Moulding Compounds (SMC), a fibre-bundle reinforced thermoset polymer composites with a matrix, which is similar to that of the BMC [1, 14, 20, 30, 34–36, 50].

Surprisingly, even if BMC's are widely used in the industry for two decades, very few studies concern their rheology during their forming process. Similarly, studies concerning the simulation of their forming are scarce. Blanc et al. [9] were the first to show that during their forming process, BMC's follow a temperature-dependent shear-thinning behaviour. This was confirmed by Kenny and Opalicki [29]. However, in these studies, BMC's were subjected to heterogenous deformation modes, so that it was not possible to propose suitable rheological models for these materials without *a priori* constitutive assumptions. More recently, Orgéas et al. [41] performed an extensive experimental study of the rheology of a BMC. BMC samples were deformed using lubricated simple compression experiments, similar to those initially proposed for SMC or other planar fibre or fibre-bundle reinforced polymer composites [20, 21, 34]. Provided both a good lubrication and samples with large dimensions (with respect to the fibre length), these tests allow the analysis of the rheology of compounds with reduced discrepancy and without any *a priori* constitutive assumptions. Doing so, the roles of the fibre content, the granulometry of the mineral filler, the current strain, the strain rate and the mechanical loading history on stress levels required to deform the studied BMC's were emphasised. In all cases, it was concluded that BMC's exhibited a pronounced and dominant non-linear viscous behaviour, with some elastic and strain-hardening effects. A simple non-linear 1D viscoelastic model was proposed to capture such effects. However, the 1D model cannot be used to simulate mould filling.

Thus, the aim of this paper is to pursue the work that has been initiated in [41] to model mould filling with BMC. For that purpose, an industrial BMC was collected at the outlet of an industrial injection machine (Section "Material"). BMC samples

were then deformed by performing lubricated simple and plane strain compression experiments (Section "Rheometers"). Experimental results underline the influence of the loading path, the current strain, as well as the imposed strain rate on recorded stress levels (Section "Experimental results"). A simple 3D non-linear viscous tensorial model is then proposed to fit these trends (Section "Proposition of a 3D tensorial model"). This model is implemented into a finite element code dedicated to the compression moulding
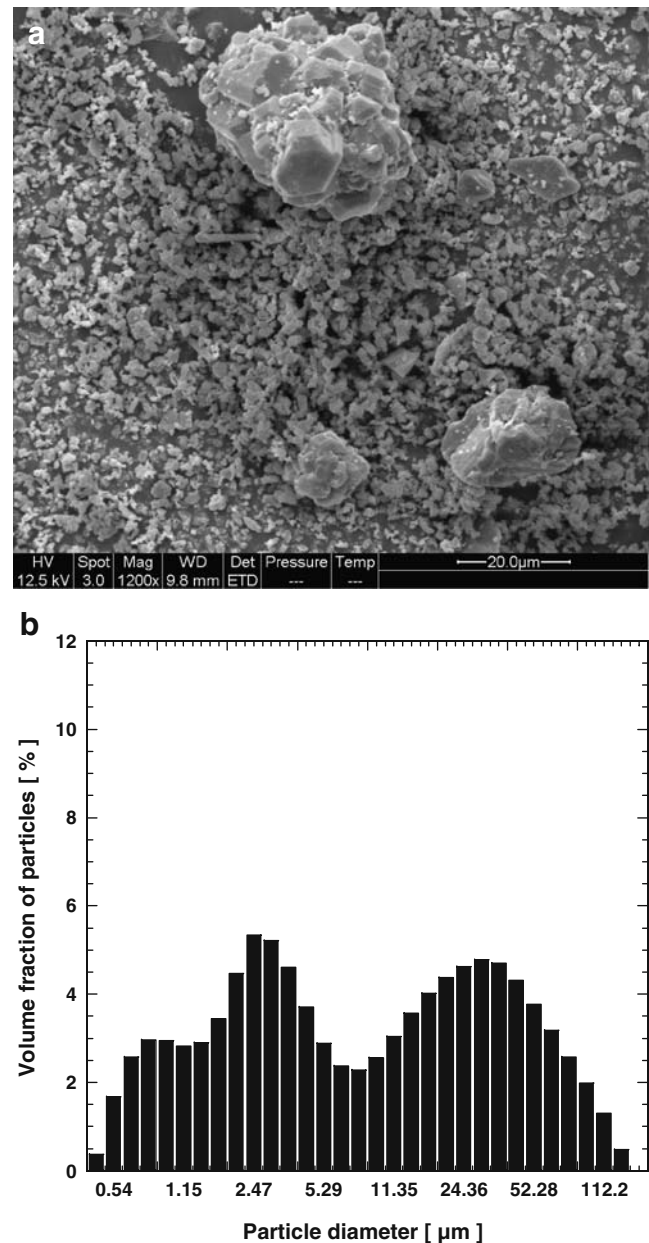

Fig. 1 SEM micrograph (**a**) and particle size distribution (obtained from a particle sizer Malvern Master Sizer X) (**b**) of the Al_2O_3 filler

of compounds. Simulation results are compared with compression experiments achieved with rather complex flow situations (Section "Mould filling simulation").

Experimental procedure

Material

The tested BMC was very close to that used in [41]. It differed from this last formulation by its longer ageing time. It was prepared and mixed by Compositec (Le Bourget-du-Lac, France). Its matrix was made up of polyester resin (35.25 wt.%), zinc stearate (2.65 wt.%), moulding agents (8.8 wt.%), and was filled with alumina (53.3 wt.%) particles. The typical aspect and size distribution are given in Fig. 1a and b, respectively. Hence, the matrix was a granular suspension with a high concentration of mineral fillers. It was then reinforced with glass-fibre bundles (initial length 6 mm, 200 fibres with a 13.7 μm diameter) at a mass fraction of 20 wt.%, which corresponded to a volume fraction of fibres of 15.4%. In order to account for the modifications entailed prior to mould filling on the fibrous microstructure of the BMC compounds (e.g. induced by the flow through an injection screw), the tested BMC was preliminary poured into an injection screw and taken at its exhaust. At this stage, fibre bundles were completely broken up, and the remaining fibres had a length comprised

Fig. 2 Distribution of the fibre length within the BMC at the exhaust of the injection press (obtained from the Morfi LB-01, TechPap)

between 0.1 and 10 mm (see Fig. 2, mean value $\approx$ 0.5 mm). They formed a complex intricate connected network where (i) no privileged orientation would be found [41] and (ii) approximately 5 to 10 fibre-fibre contacts per fibres might occur [18, 33, 45, 55] .

Rheometers

In order to characterise the rheology of the studied fibre-reinforced granular suspension, two specifically designed rheometers were used. Compared with standard commercial rheometers, these rheometers allow samples with very large dimensions to be deformed, i.e. higher than the size of the microstructure heterogeneities, thus reducing both scattering of results and possible boundary effects. These two rheometers were mounted on a mechanical testing machine (MTS 4M, load cell 20 kN, maximum cross-head velocity 8 mm s^{-1})

1. The first apparatus is the simple compression rheometer initially developed for the rheology of sheet moulding compounds [20, 34, 41]. Tests consist in compressing lubricated cylindrical samples (initial radii $R_0 = 35$ mm and 55 mm, initial height $h_0 = 20$ mm) at constant axial average strain rates $\bar{D}_{33} = \dot{h}/h$ (compression direction given by the unit vector $\underline{e}_3$) between two horizontal platens parallel to the $(\underline{e}_1, \underline{e}_2)$ plane, $(\underline{e}_1, \underline{e}_2, \underline{e}_3)$ being the usual orthogonal reference frame. During the test, the sample height h and the axial force F_3 are measured so that the average axial logarithmic strain $\bar{\varepsilon}_{33}$ and stress $\bar{\sigma}_{33}$ can be estimated by $\ln(h/h_0)$ and $F_3 h/(\pi R_0^2 h_0)$,[1] respectively (assuming the incompressibility of the studied suspensions). Provided a good lubrication of samples (here with silicone grease), a homogeneous deformation mode of samples is observed [20, 41]. Hence, the Hencky strain $\underline{\underline{\varepsilon}}$ and strain rate $\underline{\underline{D}}$ tensors can be estimated for all material points of the tested specimens:
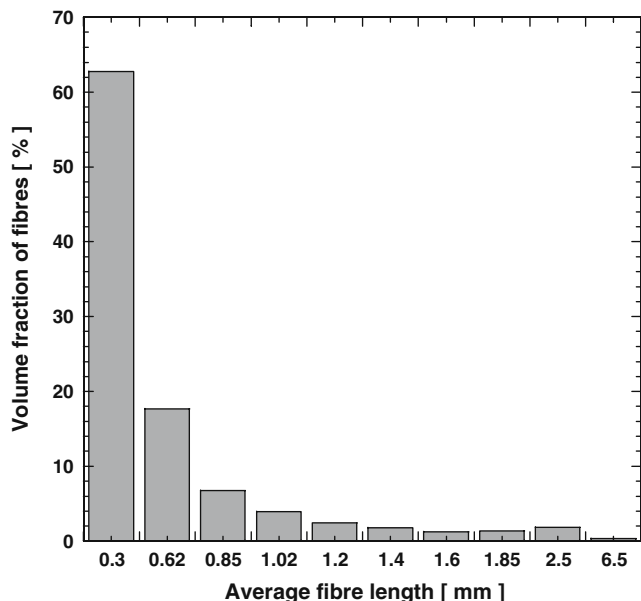
$$\underline{\underline{\varepsilon}} = \bar{\varepsilon}_{33} \left(\underline{e}_3 \otimes \underline{e}_3 - \frac{1}{2} \underline{e}_1 \otimes \underline{e}_1 - \frac{1}{2} \underline{e}_2 \otimes \underline{e}_2 \right), \qquad (1)$$

$$\underline{\underline{D}} = \bar{D}_{33} \left(\underline{e}_3 \otimes \underline{e}_3 - \frac{1}{2} \underline{e}_1 \otimes \underline{e}_1 - \frac{1}{2} \underline{e}_2 \otimes \underline{e}_2 \right). \qquad (2)$$

---

[1] In the following, compression forces, stresses, strains and strain rates will be plotted arbitrarily as positive values, by convention.

The lubrication layers between the platens and the specimen ensure the homogeneity of the flow, but they may induce friction forces, which may disturb results. This was not observed for SMC [20, 34], but was clearly established for BMC [41]. In such a case, (i) by performing two tests with two different initial radii R_0 and (ii) by assuming the lubrication layers act as Newtonian boundary layers (with a hydrodynamic friction coefficient λ), it is then possible [41] to estimate the Cauchy stress tensor:

$$\underline{\sigma} = \sigma_{33}\underline{\mathbf{e}}_3 \otimes \underline{\mathbf{e}}_3 \qquad (3)$$

with

$$\sigma_{33} = \bar{\sigma}_{33} - \frac{\lambda}{8}\frac{h_0 R_0^2}{h^3}\dot{h}. \qquad (4)$$

The friction coefficient λ was found to be close to $2\ 10^{-3}$ N s mm^{-3} for the experiments performed with the simple compression rheometer. As shown in Fig. 5a, accounting for the correction proposed by Eq. 4, stress–strain curves do not depend on the initial radii of the tested samples.

2. The second apparatus is a plane strain compression rheometer, which was recently designed [57] based on the previous one developed for SMC [20]. As shown in the simplified scheme given in Fig. 3a and the photographs displayed in Fig. 4, lubricated rectangular samples (1) (initial length along the $\underline{\mathbf{e}}_1$-direction $L_0 = 80$ mm or 160 mm, initial length along the $\underline{\mathbf{e}}_2$-direction $l_0 = 80$ mm, initial height along the $\underline{\mathbf{e}}_3$-direction $h_0 = 20$ mm) are compressed in the $\underline{\mathbf{e}}_3$-direction at constant axial average strain rates $\bar{D}_{33} = \dot{h}/h$ and forced to flow in the $\underline{\mathbf{e}}_1$-direction. During the test, the sample height h, the axial force F_3 but also the lateral force F_2 are measured, so that the average axial logarithmic strain $\bar{\varepsilon}_{33}$ and stresses $\bar{\sigma}_{33}$ and $\bar{\sigma}_{22}$ can be estimated by $\ln(h/h_0)$, $F_3 h/(L_0 l_0 h_0)$ and $F_2/(L_0 h_0)$, respectively. Notice that the lower platen (4) of this new rheometer is a 20 mm thick quenched glass plate, which allows the observation of the flow of samples, together with a CCD camera (6) positioned below it (JAI 1024×1024 pixel, 25 Hz), the flow of samples during the experiments (see Figs. 3 and 4). Once again, a good lubrication of samples allows a homogeneous sample flow [20, 57] to be obtained, so that $\underline{\varepsilon}$ and $\underline{\underline{D}}$ can be considered as uniform in the sample:

$$\underline{\varepsilon} = \bar{\varepsilon}_{33}\left(\underline{\mathbf{e}}_3 \otimes \underline{\mathbf{e}}_3 - \underline{\mathbf{e}}_1 \otimes \underline{\mathbf{e}}_1\right), \qquad (5)$$

$$\underline{\underline{D}} = \bar{D}_{33}\left(\underline{\mathbf{e}}_3 \otimes \underline{\mathbf{e}}_3 - \underline{\mathbf{e}}_1 \otimes \underline{\mathbf{e}}_1\right). \qquad (6)$$
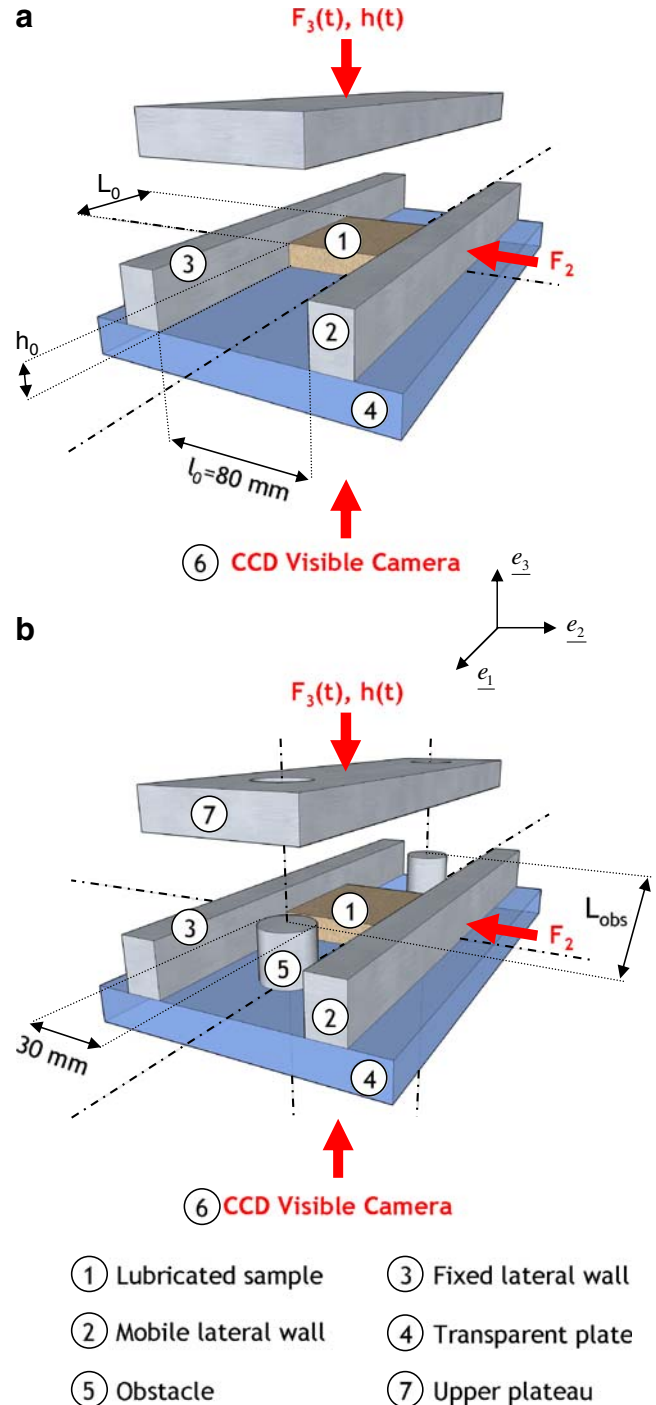

Fig. 3 Simplified schemes of the plane strain compression rheometer without (**a**) and with (**b**) cylindrical obstacles

By adopting a similar approach to the one, which is followed for the analysis of simple compression tests [41], it can be shown that the Cauchy stress tensor within flowing samples can be estimated by

$$\underline{\sigma} = \sigma_{33}\underline{\mathbf{e}}_3 \otimes \underline{\mathbf{e}}_3 + \sigma_{22}\underline{\mathbf{e}}_2 \otimes \underline{\mathbf{e}}_2 \qquad (7)$$
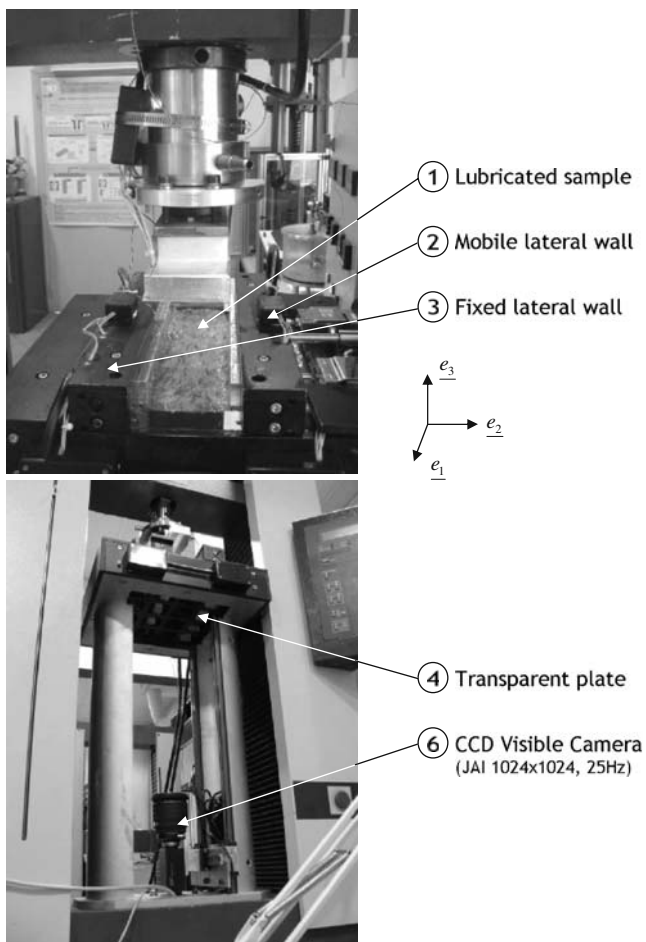
Fig. 4 Photographs of the plane strain compression rheometer

with

$$\sigma_{33} = \bar{\sigma}_{33} - \frac{\lambda}{6}\frac{L_0^2 h_0^2}{h^4}\dot{h} \text{ and } \sigma_{22} = \bar{\sigma}_{22} - \frac{\lambda}{6}\frac{L_0^2 h_0^2}{h^4}\dot{h}.$$

(8)

As shown in Fig. 5b, rather good corrections of plane strain compression curves were obtained with $\lambda = 0.8\ 10^{-3}$ N s mm^{-3}. This value is lower than that found for the simple compression rheometer, because the surface roughness is lower for the plane strain compression rheometer than for the simple compression one.

Likewise, in order to check the validity of the method proposed in this work (see Section "Mould filling simulation"), notice that this second rheometer was also modified to analyse the BMC flow in a more complex mould. This one allows the compression through a channel with two vertical cylindrical obstacles (5) (diameter = 30 mm) which can slide
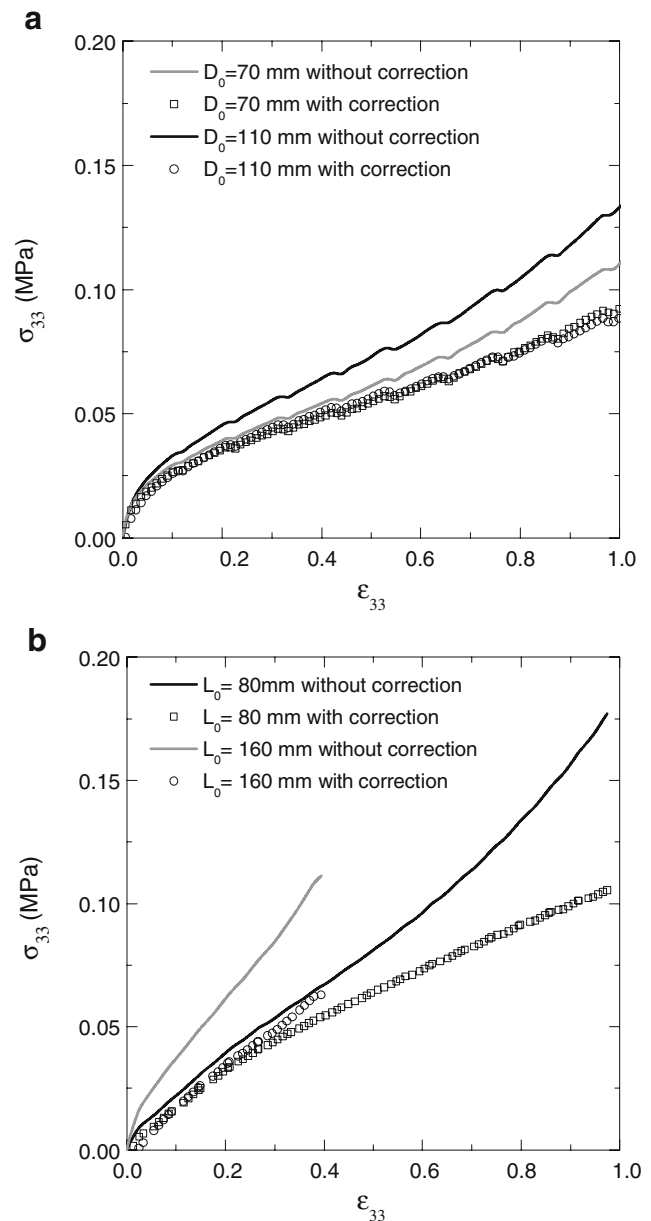

Fig. 5 Correction of simple (**a**) and plane strain (**b**) compression stress–strain curves obtained for various samples dimensions (testing temperature 25°C, axial strain rate $\bar{D}_{33} = 0.1\,\text{s}^{-1}$)

inside the upper platen (7), as depicted in Fig. 3b. The cylinders are positioned in the middle of the width of the channel at a distance $L_{obs} = 180$ mm.

Sample preparation and testing conditions

To produce simple and plane strain compression samples, the following method was strictly observed in

order to get samples for which it could be assumed they had the same initial fibrous microstructure:

– a prescribed amount of BMC was taken from bags and hand-mixed in order to induce fibrous microstructures with random fibre orientation and to pre-shape thin cylindrical (for simple compression) or thin rectangular samples (for plane strain compression) close to their final dimensions. The pre-shaping flattens BMC, leading to a preferential fibre orientation within the principal plane of the sample (of normal unit vector $\underline{\mathbf{e}}_3$).
– pre-shaped samples were then put into cylindrical or rectangular moulds and compressed at a closing force of 20 kN in order to adjust the final sample dimensions. During such a nearly œdometric compaction, the flow of the BMC was limited, so that the sample microstructure was unlikely to evolve.

Thus, the fibrous microstructures of produced samples initially exhibited transverse isotropy, the symmetry axis of which was parallel to the compression axis $\underline{\mathbf{e}}_3$. Therefrom, samples were then placed into the rheometers and deformed at room temperature (25°C) and at constant average axial strain rate $\bar{D}_{33}$ ranging from 10^{-3} to 10^{-1} s^{-1}.

Experimental results

Typical stress–strain curves obtained during simple or plane strain compression experiments are plotted in Figs. 5 and 6.

As evident from these figures, whatever the mechanical loading and whatever the considered strain rate, the stress–strain curves exhibit a noteworthy strain hardening. The first stress increase, i.e. when $\varepsilon_{33} < 0.25$, can be due to viscoelastic effects [41]. Above, the stress increase is approximately 300% to 1000% when the strain rises from 0.25 to 1. Such a hardening may be induced (i) by the rearrangement of the mineral particles and the polymer within the matrix and (ii) by the alignment of the glass fibres along the flow direction. In order to gauge the importance of these two possible mechanisms, two graphs have been plotted in Fig. 7:

* Graph (a) is built from the simple compression experiments performed in [41]. For this type of flow, the initial nearly planar random fibrous microstructure should not evolve drastically [13, 21]. The graph represents the evolution of the normalised stress σ^* as a function of the axial strain ε_{33}, during the simple compression at $D_{33} = 0.1$ s^{-1} of two BMC's with a fibre content of 10 wt.% and 20 wt.%.
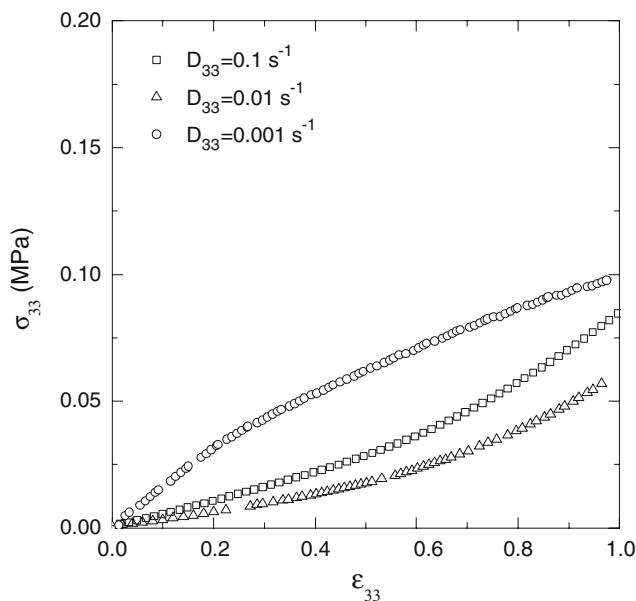
Fig. 6 Evolution of the axial stress σ_{33} with the axial strain $\bar{\varepsilon}_{33}$ during plane strain compressions performed at different strain rates $\bar{D}_{33}$

The dimensionless axial stress σ^* corresponds to the axial stress σ_{33} recorded for those BMC's divided by the axial stress σ_{33} recorded for the BMC without fibre (fibre content = 0 wt.%). As shown from this graph, whatever the investigated fibre content, the dimensionless stress σ^* is more or less constant. An identical trend was also noticed during the flow of fibre reinforced mortars, which displayed a microstructure and a rheology rather close to the BMC one [13]. Hence, the strain-hardening observed in simple compression is mainly due to the pasty matrix, e.g. to a rearrangement of the mineral particles and the polymer during the flow.

* Graph (b) is built from the simple and plane strain compression experiments shown in Fig. 5, i.e. with the same material. In this case, σ^* corresponds to the axial stress σ_{33} recorded during the plane strain compression divided by the axial stress σ_{33} recorded during the simple compression. As seen in this graph, a slight increase of σ^* is observed, of about 20%. Such a trend follows that observed during the elongation of standard polymer suspensions reinforced with fibres (e.g. [25]), it is due to the evolution of the fibre orientation along the flow direction $\underline{\mathbf{e}}_1$ during the plane strain compression [21]. It is also of the same order of magnitude as that predicted by the micro-macro model developed in [33] for SMC. Anyway, the strain hardening that fibre orientation evolution can induce is much smaller than the one, which is induced by the local
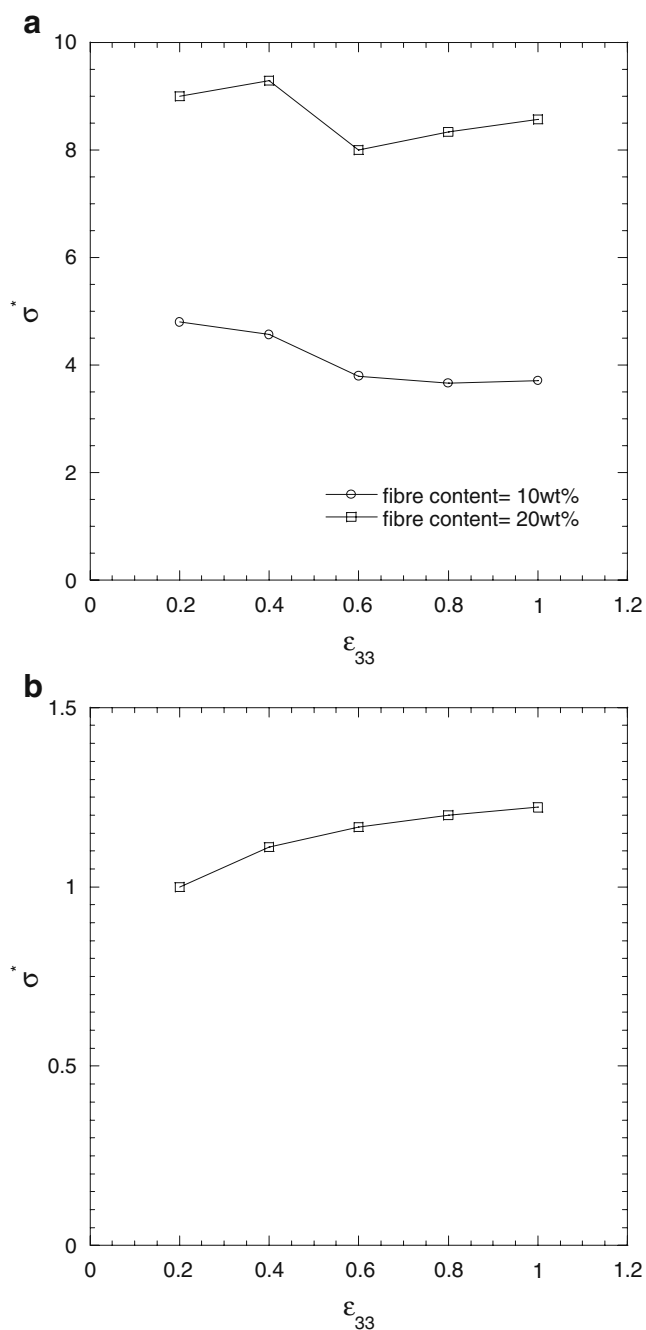
Fig. 7 Evolution of the dimensionless stress σ^* with the axial strain $\bar{\varepsilon}_{33}$ when $\bar{D}_{33} = 0.1\ s^{-1}$. σ^* is estimated from simple compression experiments performed in [41] (**a**) and compressions (simple and plane strain) performed in this work (**b**)

the axial plane strain stress σ_{33} recorded at two axial strains ε_{33}, i.e. 0.25 and 0.8. In both cases, the viscosity is a power-law function of the strain rate D_{33}, i.e. $\eta_{33} = \eta_{33}^0 D_{33}^{n-1}$. The consistency η_{33}^0 and the strain rate sensitivity n are respectively equal to 0.09 MPa s^n and 0.22 MPa s^n and to 0.34 and 0.22, when $\varepsilon_{33} = 0.4$ and 0.8, respectively. A very similar trend has been reported previously [41], even for the BMC without fibre. Thus, both the decrease of n with ε_{33} and the strain hardening (which implicitly induces an increase of the consistency η_{33}^0) are mainly due to a rearrangement of the mineral fillers and the polymer during the flow. For instance, as the compression is increased, the Newtonian polymer, which is between contacting particles and which acts as a lubricant, may be progressively expelled from contacting zones so that associated lubrication forces will be lowered with respect to Coulombic friction forces [15]. This would be a possible scenario occurring at the microscale.

For plane strain compression tests, the stress ratio σ_{33}/σ_{22} is a decreasing function of the axial strain ε_{33}, as evident from Fig. 9b. This evolution is also related to the evolution of the BMC microstructure (i.e. polymer matrix and fibres) during the flow. Nonetheless, it is important to notice from the same figure that the stress ratio does not depend on the imposed strain rate D_{33} since the curves are nearly superimposed.
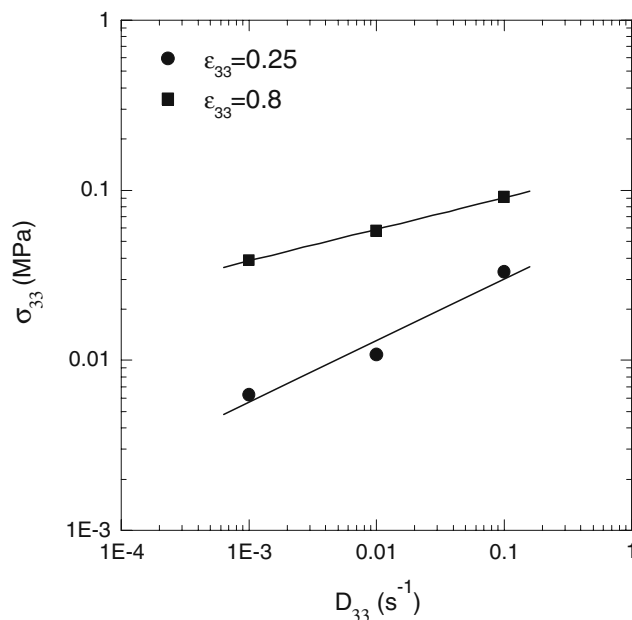
Fig. 8 Plane strain compression results. Evolution of the axial stress σ_{33} recorded at two axial strains ($\bar{\varepsilon}_{33} = 0.25$ and 0.8) with respect to the axial strain rate $\bar{D}_{33}$ (continuous lines are the power-laws used to fit the data)

deformation of the pasty matrix, at least for the investigated testing conditions.

The imposed axial strain rate D_{33} also plays a significant influence, as shown in Fig. 6, which emphasises the strong viscous behaviour of the tested BMC. To better underline this, Fig. 8 reports the evolution of

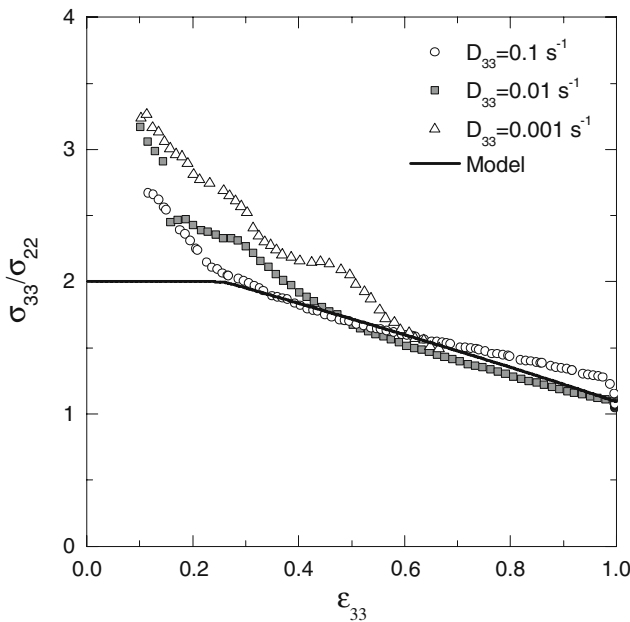**Fig. 9** Evolution of the stress ratio σ_{33}/σ_{22} during the plain strain compressions plotted in Fig. 6. The continuous line represents the prediction of the proposed model

Proposition of a 3D tensorial model

Model definition

On the basis of the previous experimental results, a 3D tensorial model is proposed to model the rheology of BMC. For the sake of simplicity, we neglect viscoelastic effects associated with the rheology of BMC [41]. In particular, such effects are mainly responsible for the stress increase observed for monotonic loading at axial strain below a characteristic value $\varepsilon_c \approx 0.25$. Instead, we assume that the considered BMC can be seen as a one-phase viscous and incompressible continuum. Its corresponding stress tensor $\underline{\underline{\sigma}}$ is therefore written as

$$\underline{\underline{\sigma}} = -p\underline{\underline{\delta}} + \underline{\underline{\sigma}}^v, \tag{9}$$

where p, $\underline{\underline{\delta}}$ and $\underline{\underline{\sigma}}^v$ are the incompressibility pressure, the identity tensor and the viscous stress tensor, respectively. As already proposed previously for SMC [20], $\underline{\underline{\sigma}}^v$ is assumed to be the partial derivative of a volumetric viscous dissipation potential Ω with respect to the strain rate tensor $\underline{\underline{D}}$. Ω is supposed to be a convex and positive function of $\underline{\underline{D}}$ and it is such that $\partial\Omega/\partial\underline{\underline{D}} = \underline{\underline{0}}$ when $\underline{\underline{D}} = \underline{\underline{0}}$. We further assume that Ω can be written as a function of a positive scalar equivalent strain $D_{eq}(\underline{\underline{D}})$. Thus,

$$\underline{\underline{\sigma}}^v = \frac{\partial\Omega}{\partial\underline{\underline{D}}} = \frac{\partial\Omega}{\partial D_{eq}}\frac{\partial D_{eq}}{\partial\underline{\underline{D}}} = \sigma_{eq}\frac{\partial D_{eq}}{\partial\underline{\underline{D}}}, \tag{10}$$

where the equivalent stress σ_{eq} is associated with the equivalent strain rate D_{eq} by the following expression:

$$P_{dis} = \underline{\underline{\sigma}}^v : \underline{\underline{D}} = \sigma_{eq}D_{eq}, \tag{11}$$

P_{dis} being the volumetric mechanical dissipation. The experimental results shown in the previous section lead to propose the following constitutive equation, in order to account for the observed strain-hardening and non-linear viscous effects:

$$\sigma_{eq} = \eta_0 e^{k\varepsilon_{eq}} D_{eq}^n, \tag{12}$$

where the consistency η_0, the strain-hardening coefficient k and the power-law exponent n are constitutive parameters and where the equivalent strain ε_{eq} is defined as:

$$\varepsilon_{eq} = \int_0^t D_{eq}\mathrm{d}t \quad \text{or} \quad \frac{\mathrm{d}\varepsilon_{eq}}{\mathrm{d}t} = D_{eq}, \tag{13}$$

where the symbol $\mathrm{d}/\mathrm{d}t$ represents the material time derivative. The choice of the equivalent strain rate D_{eq} is open. In the next section, the compression moulding of thin BMC plates is addressed, with an initial fibrous microstructure, which is mainly aligned along the midplane $(\underline{e}_1, \underline{e}_2)$ of the plates. Results gained in the previous section showed that the mechanical behaviour of the BMC was not strongly affected by the fibre orientation evolution (see Fig. 7), at least compared with the impact of the strain-hardening of the pasty matrix. Thus, it seems reasonable to assume, as a first approximation, that the mechanical behaviour of the considered BMC does not depend on the fibre orientation evolution and exhibits transverse isotropy, the privileged direction $\underline{e}_3$ of which is the normal to the midplane of the plate. In this situation, a possible form of D_{eq} is [20, 39]:

$$D_{eq}^2 = \alpha_0 \left(\underline{\underline{D}} : \underline{\underline{D}} + \alpha_1(\underline{\underline{M}} : \underline{\underline{D}})^2 + \alpha_2(\underline{\underline{D}} \cdot \underline{\underline{M}}) : \underline{\underline{D}}\right) \tag{14}$$

with

$$\begin{cases} \alpha_0 = \frac{2}{1+2H} \\ \alpha_1 = 1 + H - 2\frac{1+2H}{3L} \\ \alpha_2 = 2\left(\frac{1+2H}{3L} - 1\right) \end{cases} \tag{15}$$

and where $\underline{\underline{M}} = \underline{e}_3 \otimes \underline{e}_3$ is the microstructure tensor characterising the transverse isotropy of the material [10]. $H > -0.5$ and $L > 0$ are two additional constitutive parameters. Their physical meaning can be expressed as follows: for the same given mechanical dissi-

pation P_{dis}, the BMC flow occurs when $\sigma_{eq} = \sigma_{33}$, $\sigma_{eq} = \sqrt{(1+H)/2}\,\sigma_{11}$ and $\sigma_{eq} = \sqrt{3L}\,\sigma_{31}$ when the BMC is subjected to a simple compression along $\underline{e}_3$, a simple compression along $\underline{e}_1$, and a shear in the $(\underline{e}_1, \underline{e}_3)$ plane, respectively. Please also notice that the above expression of D_{eq} is such that its associated dual variable, i.e. the equivalent stress σ_{eq}, equals the well-known Hill yield criterion [27] established for elastic-plastic materials exhibiting a transverse isotropy along the $\underline{e}$ direction ($\underline{e} = \underline{e}_3$ here). Hence, the combination of the previous expressions leads finally to the following form of the viscous stress tensor:

$$\underline{\underline{\sigma}}^v = \alpha_0 \eta_0 e^{k\varepsilon_{eq}} D_{eq}^{n-1} \left(\underline{\underline{D}} + \alpha_1 (\underline{\underline{M}} : \underline{\underline{D}}) \underline{\underline{M}} \right.$$
$$\left. + \tfrac{\alpha_2}{2} (\underline{\underline{D}} \cdot \underline{\underline{M}} + \underline{\underline{M}} \cdot \underline{\underline{D}}) \right). \tag{16}$$

The influence of the fibre orientation evolution was neglected (as a first approximation) in the above constitutive equations, compared with the strong influence of the pasty matrix on the rheological behaviour (see above). However, fibre orientation may play a role on the final mechanical and physical properties of produced composites parts (e.g. [42]). Hence, in order to estimate the flow-induced fibre orientation, the above set of constitutive equations is completed with a standard modified Jeffery's equation [26, 28]. This equation is expressed (i) by assuming that fibres are very slender with a planar orientation along $(\underline{e}_1, \underline{e}_2)$ (ii) by assuming that the BMC follows a plug flow along the midplane $(\underline{e}_1, \underline{e}_2)$ of the considered plates during forming (see below), and (iii) by using the in-plane second order $\tilde{\underline{\underline{A}}}$ and fourth order $\tilde{\underline{\underline{\underline{\underline{A}}}}}$ fibre orientation tensors [2]:

$$\frac{\mathrm{d}}{\mathrm{d}t} \tilde{\underline{\underline{A}}} = \tilde{\underline{\underline{\Omega}}} \cdot \tilde{\underline{\underline{A}}} - \tilde{\underline{\underline{A}}} \cdot \tilde{\underline{\underline{\Omega}}} + \tilde{\underline{\underline{A}}} \cdot \tilde{\underline{\underline{D}}} + \tilde{\underline{\underline{D}}} \cdot \tilde{\underline{\underline{A}}}$$
$$+ \tilde{\underline{\underline{\underline{\underline{A}}}}} : \tilde{\underline{\underline{D}}} + 2 C_I \tilde{\gamma} \left(\tilde{\underline{\underline{\delta}}} - 2 \tilde{\underline{\underline{A}}} \right). \tag{17}$$

where $\tilde{\underline{\underline{\Omega}}}$ and $\tilde{\gamma}$ are respectively the in-plane vorticity tensor and equivalent shear strain rate, and where C_I is a constitutive parameter that accounts for fibre-fibre interactions [26]. The fourth order fibre orientation tensor involved in the last equation is expressed as a function of the second order fibre orientation tensor, by using the 2D natural closure approximation [22]. Hence, in $(\underline{e}_1, \underline{e}_2)$, this yields to $(i, j, k, l = 1, 2)$:

$$\tilde{A}_{ijkl} = \frac{1}{3} \left(\tilde{A}_{ij} \tilde{A}_{kl} + \tilde{A}_{ik} \tilde{A}_{lj} + \tilde{A}_{il} \tilde{A}_{jk} \right)$$
$$+ \frac{1}{6} \left(\delta_{ij} \delta_{kl} + \delta_{ik} \delta_{lj} + \delta_{il} \delta_{jk} \right) \det \tilde{\underline{\underline{A}}}. \tag{18}$$

Please note that the microstructure tensor $\underline{\underline{M}}$ is not equivalent to the second order fibre orientation tensor $\tilde{\underline{\underline{A}}}$. For the considered BMC's, fibrous microstructures are mainly aligned in the principal plane of the samples. The normal of this plane is a preferred direction and the microstructure tensor accounts for it in the rheological model. For the flow situations considered in this work, the principal plane of the samples is invariant, so that there is no need to update the microstructure tensor.

Identification of constitutive parameters

With the help of the simple and plane strain compression tests performed in the previous section, for which $\underline{e} = \underline{e}_3$, it is possible to determine five of the six constitutive parameters of the model, i.e. η_0, k, n, H and C_I. For the flow kinematics that will be considered in the next section, i.e. plug flows, notice that it is not necessary to determine the last constitutive parameter L, which could have been determined shear tests in the $(\underline{e}_1, \underline{e}_3)$ plane [20, 34].

- The interaction coefficient C_I was set to 0.005. This value corresponds to the average value of those used in the literature for fibre suspensions displaying similar fibre content and aspect ratio [8, 43, 46].
- From the plane strain compression experiments, H can be directly deduced from the stress ratio σ_{33}/σ_{22} since

$$\frac{\sigma_{33}}{\sigma_{22}} = 1 + H. \tag{19}$$

Results reported in Fig. 9 show that H should depend on the strain. To take this into account, H was taken as a function of the equivalent strain ε_{eq}:

$$H = 1 - \frac{\mu}{2} \left(\varepsilon_{eq} + \sqrt{(\varepsilon_{eq} - \varepsilon_c)^2 + \alpha^2} - \sqrt{\varepsilon_c^2 + \alpha^2} \right), \tag{20}$$

where the characteristic strain ε_c, the slope μ and the curvature α were set to 0.25, 1 and 0.01, respectively. As shown in the graph of Fig. 9, such an expression allows a reasonable fit of experimental data for strain above 0.25. Below this value, viscoelastic effects occur and are not accounted for in the present model: in this strain domain, H was arbitrarily fixed to the value obtained near $\varepsilon_{eq} = 0.25$. Likewise, above the equivalent strain equal to 1, H was also fixed arbitrarily to $H(\varepsilon_{eq} = 1)$, in the absence of experimental data.

- From the axial stresses recorded during the compression experiments performed at various axial strain rates, η_0, k and n can be estimated. For

example, the axial stress σ_{33} for simple compression is:

$$\sigma_{33} = \eta_0 e^{k\varepsilon_{33}} D_{33}^n. \tag{21}$$

Doing so, within the investigated strain and strain rate ranges, the following values were determined:

$$\eta_0 = 0.07 \text{ MPa s}^n, \, k = 0.5, \, n = -0.23\varepsilon_{eq} + 0.41. \tag{22}$$

a

b

Once again, in the absence of experimental data above $\varepsilon_{eq} > 1$, n was arbitrarily fixed to $n(\varepsilon_{eq} = 1)$.

Stress–strain curves plotted in Fig. 10 show the comparison between the model prediction and the experimental data collected during various simple and plane strain compression experiments. Together with the stress ratios shown in Fig. 9, these graphs indicate that the model permits a fairly good fit of experimental results, whatever the considered mechanical loading. Of course, experimental and model curves differ in their early stage, i.e. when $\varepsilon_{eq} < 0.25$, because the very simple proposed model does not account for viscoelastic effects observed experimentally [41].

Mould filling simulation

Finite Element code for compression moulding

The previous rheological model was then implemented into a Finite Element (FE) code able to simulate the compression moulding of thin SMC or BMC charges. Mechanical and numerical aspects related to this code are extensively described in [19]. Briefly, the flow of the compound during the compression is supposed to be equivalent to an incompressible and one-phase plug flow [1, 7], so that the velocity of the suspension along the thickness of the BMC charge is uniform. Hydrodynamic friction forces having the same effects than those used to correct stress measurements during homogeneous compression experiments (cf. Section "Experimental procedure") can also be taken into account. Hence, only the midplane of the mould cavity is considered, and by following an Eulerian description, the whole mould is meshed (see Fig. 11). The flow problem (mass balance and quasi-static momentum balance equations + constitutive Eqs. 9–16) is then treated using a mixed pressure-velocity formulation (modified Uzawa algorithm + Newton Raphson linearisation, P2+/P1 FE elements). The evolution of the flow front during the compression is solved using a level set function, which is advected by a characteristic-based method and P2 FE elements. In order to compute the equivalent strain ε_{eq} and the fibre orientation tensor $\underline{\underline{\tilde{A}}}$ at each material point during the flow, similar resolution schemes are also implemented for the weak forms of Eqs. 13b and 17, respectively.

Comparison experiments / simulation results

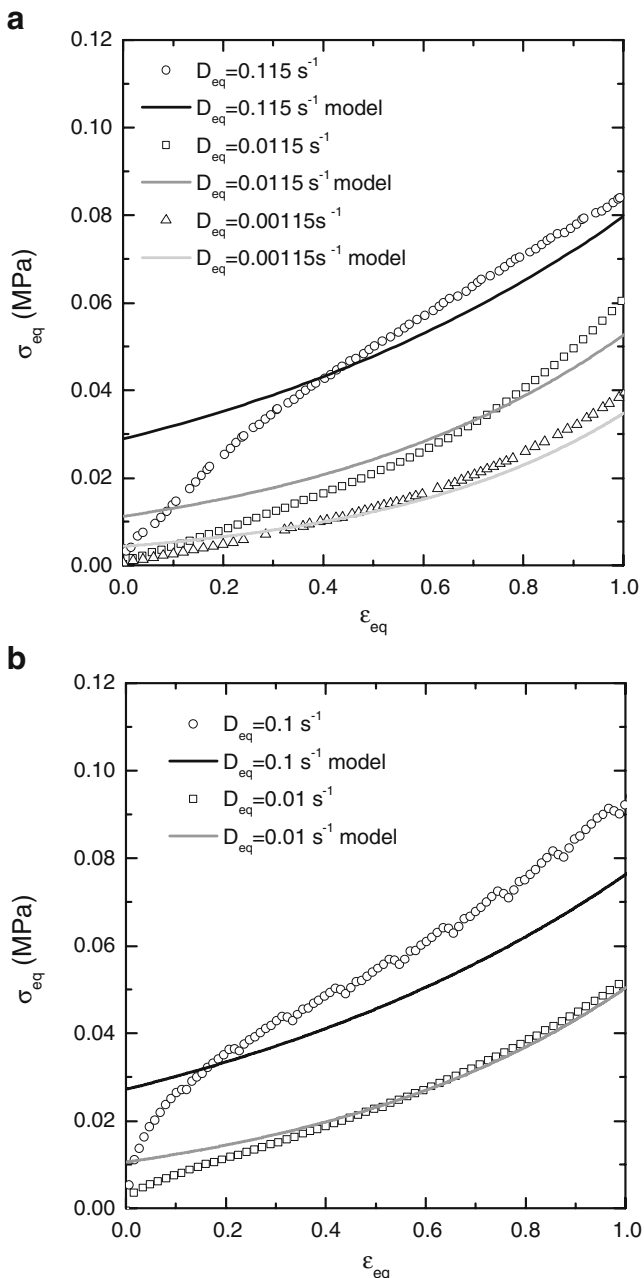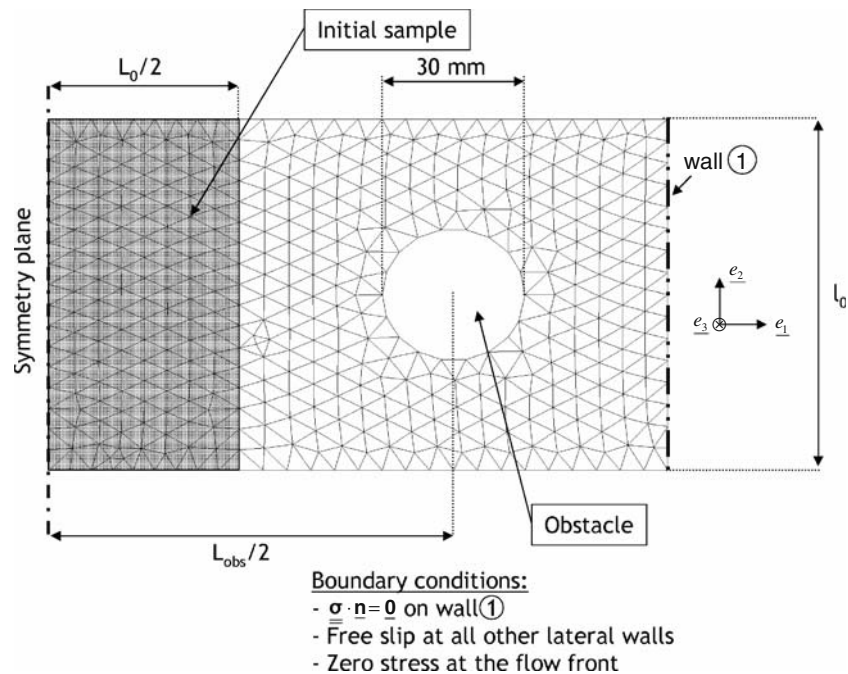To test the capability of the FE code to simulate complex flow situations, the compression experiments in the

Fig. 10 Stress–strain curves showing a comparison between the model prediction (*continuous lines*) and the experiments (*marks*) during plane strain (**a**) and simple compression experiments (**b**)

Fig. 11 Geometry, mesh, position of the initial BMC charge and boundary conditions used to run simulation

Boundary conditions:
- $\underline{\underline{\sigma}} \cdot \underline{n} = \underline{0}$ on wall ①
- Free slip at all other lateral walls
- Zero stress at the flow front

channel with the obstacles are now considered. During the tests, the CCD camera is used in order to capture the BMC flow front. The samples used in this case are rectangular (dimensions $L_0 \times l_0 \times h_0 = 80 \times 80 \times 20$ mm^3). They are initially lubricated and placed in the centre of the channel. They are then compressed at constant axial strain rate and three initial cross-head velocities equal to 0.2, 2 and 6 mm s^{-1}. Tests are performed at room temperature. It must be pointed out that such testing conditions, despite their simplicity, are not so far from the industrially encountered ones. Indeed, during the short duration of the compression mouldings, it is fair to assume [5] that the temperature of the compounds (i) is sufficiently low to avoid curing of the polymer and (ii) is approximately constant except near the lower and upper parts of the mould, where the heated polymer matrix acts as a lubricant [6, 11, 31, 40, 44].

In parallel, the same compression experiments are simulated with the FE code together with the rheological model developed in this work. The geometry, the mesh, the initial and boundary conditions are given in Fig. 11. The comparison between the experiments and the simulation results is presented in Fig. 12. This figure brings up the following comments:

– The pictures taken with the CCD camera at various times during the compression at the initial cross-head velocity of 2 mm s^{-1} (see Fig. 12c) together with the snapshots extracted from the corresponding simulation at the same times prove that the

simulated flow fronts fit fairly well the experimental ones.

– When the simulations are performed both with the rheological model, which has been proposed in the previous section, and with the hydrodynamic friction coefficient λ, which has been determined for the plane strain compression rheometer (*cf.* Subsection "Rheometers"), the experimental force-height curves are well reproduced, whatever the initial cross-head velocity, as shown in the graph of Fig. 12a. The best correspondence is obtained whenever the equivalent strain ε_{eq} remains below 1 and becomes deteriorated when $\varepsilon_{eq} \geq 1$. This constitutes a limitation of the presented model as the identification of its parameters has not been performed when $\varepsilon_{eq} \geq 1$, as previously explained. This point should be further improved. In the particular studied flow, a state of equivalent strain $\varepsilon_{eq} \geq 1$ is reached quite rapidly around the cylindrical obstacles, as it is illustrated in Fig. 12c in the case of an initial cross-head velocity of 2 mm s^{-1}.

– In order to gauge the effect of constitutive parameters on the simulation, different runs have also been achieved in the case of the compression at the initial cross-head velocity of 2 mm s^{-1}, see Fig. 12b. As evident and shown from the simulations achieved without friction, neglecting the strain-hardening ($k = 0$) leads to the lowest mould closure force F. Adding both the effects of the friction and the strain hardening leads to the highest closure force. It is 1.5 times higher than the previous value at half

Fig. 12 Compression in the channel with cylindrical obstacles : comparison between experiments and simulations when the initial compression velocity equals 2 mm s^{-1} and when it equals 0.2 mm s^{-1} and 6 mm s^{-1} (**a**). Graphs represent the mould closure force F as a function of the height h of the mould cavity. *Marks* represent the experimental data and lines predictions given by the simulations. Graph (**b**) represents the influence of constitutive parameters on the mould closure force (initial compression velocity equals 2 mm s^{-1}). Photographs (experiment on top, simulation on bottom) shown in (**c**) represent the bottom view of the mould. They were taken at various times (1,2,3,4) during the compression at 2 mm s^{-1}. Colormaps shown in the numerical pictures represent the equivalent strain ε_{eq} and the first principal component A_I of the orientation tensor, from zero (*red*) to the maximal value (*white*)
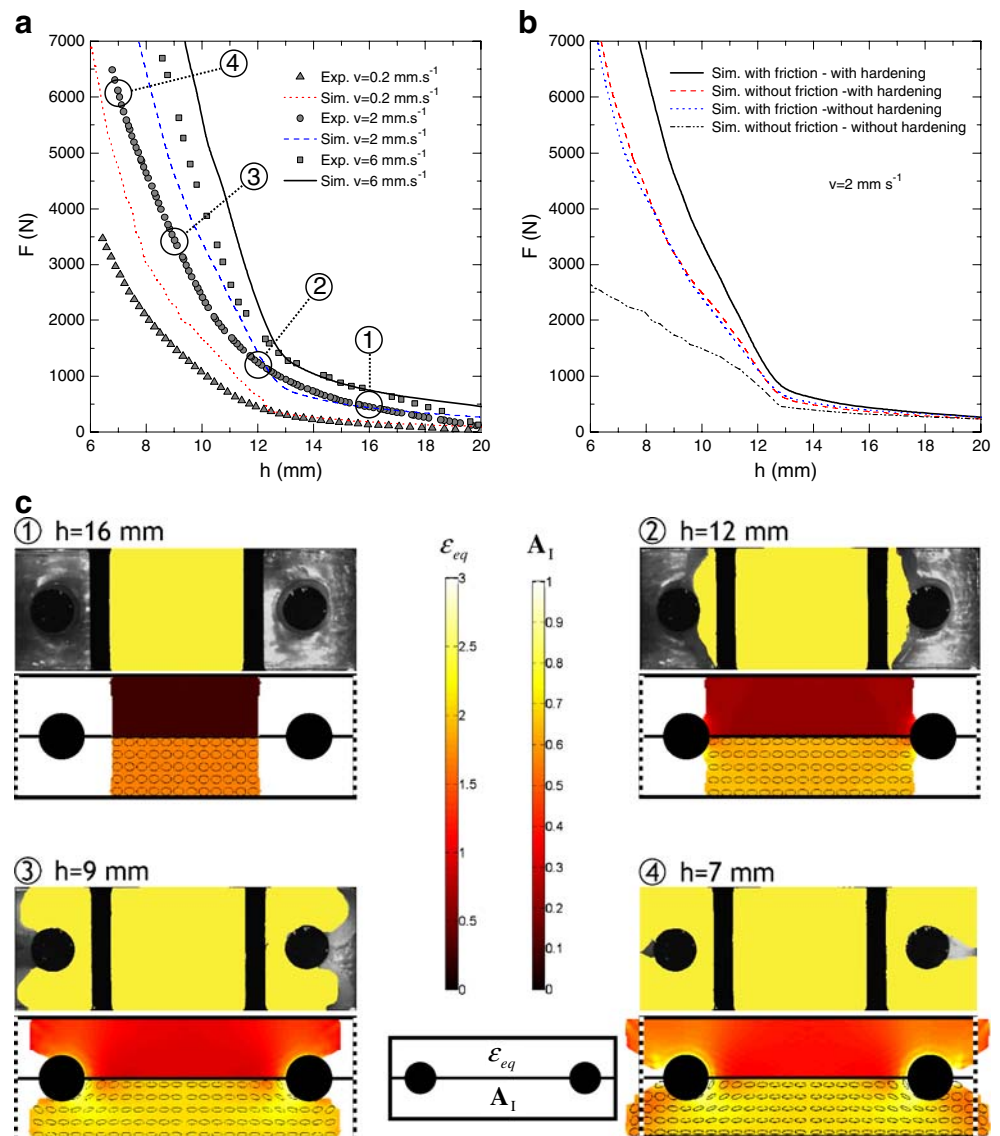
the compression and triples near the end of the compression. Considering the individual effects of the friction or the strain hardening leads to closure force values comprised between the two previous cases and of close magnitudes, showing both the importance of the bulk rheological behaviour of the BMC and of its interaction with the mould surfaces.

– At least, the evolution of the first principal value A_I of the fibre orientation tensor and the corresponding orientation ellipses (they are aligned with the principal 2D reference frame and their major and minor axes are respectively equal to A_I and $A_{II} = 1 - A_I$) are given in Fig. 12c in the case of an initial cross-head velocity of 2 mm s^{-1}. This graph shows an overall alignment of the fibres along

the channel axis, with a complex orientation when the BMC flows around the cylindrical obstacles. An interesting analysis, which would have to be performed, would consist in determining experimentally the orientation state of fibres around these obstacles and to compare it with these numerical results. Nevertheless, this work cannot be easily performed with BMC materials. It would require special observation techniques developed in [53] or [31], for instance.

Conclusion

– The analysis, which was initiated in [41] in order to understand the rheology of Bulk Moulding

Compounds, was pursued. Once again, results have shown that these polymer composites behave as highly concentrated fibre-reinforced non-Newtonian suspensions during their forming phase, exhibiting a complex rheology. In particular, the role of the mechanical loading on the suspension rheology was emphasised, by performing both simple and plane strain compression experiments using large size rheometers. This database could be completed by shear tests such as those achieved in [34], since shear is another important deformation mode arising during processing of BMC's. In order to better understand the BMC rheology, an important work should also be carried out about the analysis of their microstructures, which are induced during the flow [14, 31, 53].

– As a quick answer towards the modelling of mould filling, a mesoscopic phenomenological tensorial rheological model is proposed. This model requires few constitutive parameters, and reproduces the main features of the BMC rheology. However, it is not able to relate finely the BMC's rheology with their microstructures. Based on an experimental analysis of flow-induced microstructures, such a model could be in future replaced by more sophisticated rheological models dedicated to these types of fibre suspensions [4, 24, 32, 33, 38, 51, 52, 56, 58].

– This phenomenological model was implemented into a FE code dedicated to the compression of compounds [19]. Compared to heterogeneous compression moulding experiments, rather good trends were obtained from simulation. Future work should now focus on simulating more complex geometries and more complex situations combining thermal and mechanical loads.

References

1. Abrams L, Castro J (2003) Predicting molding forces during sheet molding compound (SMC) compression molding. I: Model development. Polym Compos 24:291–303

2. Advani SG, Tucker CL (1987) The use of tensors to describe and predict fiber orientation in short fiber composites. J Rheol 3(8):751–784

3. Ausias G, Agassant JF, Vincent M, Lafleur PG, Lavoie PA, Carreau PJ (1992) Rheology of short glass fiber reinforced polypropylene. J Rheol 36:525–542

4. Ausias G, Fan X, Tanner R (2006) Direct simulation for concentrated fibre suspensions in transient and steady state shear flows. J Non-Newton Fluid Mech 135:46–57

5. Barone M, Caulk D (1979) The effect of deformation and thermoset cure on heat conduction in a chopped-fiber reinforced polyester during compression molding. Int J Heat Mass Transfer 22(7):1021–1031

6. Barone M, Caulk D (1985) Kinematics of flow in sheet molding compound. Polym Compos 6(2):105–109

7. Barone MR, Caulk DA (1986) A model for the flow of a chopped fiber reinforced polymer compound in compression molding. J Appl Mech 53(191):361–370

8. Bay SR, Tucker CL (1992) Fiber orientation in simple injection moldings. Part i: theory and numerical methods. Polym Compos 13(4):317–331

9. Blanc R, Agassant JF, Vincent M (1992) Injection molding of unsaturated polyester compounds. Polym Eng Sci 32(19):1440–1450

10. Boelher JP (1987) Applications of tensor functions in solids mechanics. Springer, New York

11. Boylan S, Abrams LM, Castro JM (2003) Predicting molding forces during sheet molding compound (SMC) compression molding. II: effect of SMC composition. Polym Compos 24(6):731–747

12. Caba A, Loos A, Batra R (2007) Fiber-fiber interaction in carbon mat thermoplastics. Compos Part A 38:469–483

13. Chalencon F, Orgéas L, Dumont PJJ, Foray G, Cavaillé J-Y, Maire E, Rolland du Roscoat S (2009) Lubricated compression and x-ray microtomography to analyse the rheology of a fibre-reinforced mortar. Rheol Acta (in press)

14. Comte E, Mehri D, Michaud V, Månson J-A (2006) Void formation and transport during SMC manufacturing: effect of the glass fiber sizing. Polym Compos 27:289–298

15. Coussot P, Ancey C (1999) Rheophysical classification of concentrated suspensions. Phys Rev E 59:4445–4457

16. Djalili-Moghaddam M, Toll S (2005) A model for short-range interactions in fibre suspensions. J Non-Newton Fluid Mech 132:73–83

17. Djalili-Moghaddam M, Toll S (2006) Fibre suspension rheology: effect of concentration, aspect ratio and fibre size. Rheol Acta 45:315–320

18. Doi M, Edwards SF (1978) Dynamics of rod-like macromolecules in concentrated solution. J Chem Soc Faraday Trans II 74(1):560–570

19. Dumont P, Orgéas L, Favier D, Pizette P, Venet C (2007) Compression moulding of SMC: in situ experiments, modelling and simulation. Compos Part A 38:353–368

20. Dumont P, Orgéas L, Le Corre S, Favier D (2003) Anisotropic viscous behaviour of sheet molding compounds (SMC) during compression molding. Int J Plast 19(4):625–646

21. Dumont P, Vassal J-P, Orgéas L, Michaud V, Favier D, Månson J-A E (2007) Processing, characterization and rheology of transparent concentrated fibre bundle suspensions. Rheol Acta 46:639–651

22. Dupret F, Verleye V (1999) Modelling the flow of fiber suspensions in narrow gaps. Rheology Series. Elsevier, Amsterdam, pp 1347–1398

23. Dweib MA, Ó Brádaigh CM (1999) Extensional and shearing flow of a glass-mat-reinforced thermoplastics (GMT) material as a non-newtonian viscous fluid. Compos Sci Technol 59:1399–1410

24. Fan X, Phan-Thien N, Zheng R (1998) A direct simulation of fibre suspensions. J Non-Newton Fluid Mech 74:113–135

25. Férec J, Heuzey M-C, Pérez-González J, de Vargas L, Ausias G, Carreau PJ (2009) Investigation of the rheological properties of short glass fiber-filled polypropylene in extensional flow. Rheol Acta 48:59–72

26. Folgar F, Tucker CL (1984) Orientation behavior of fibers in concentrated suspensions. J Reinf Plast Compos 3:98–118

27. Hill R (1950) Mathematical theory of plasticity, Oxford university press edition. Oxford University Press, Oxford
28. Jeffery GB (1922) The motion of ellipsoidal particles immersed in a viscous fluid. Proc R Soc Lond A 102:161–179
29. Kenny J, Opalicki M (1996) Processing of short fibre/thermosetting matrix composites. Compos Part A 27A(3):229–240
30. Kotsikos G, Gibson AG (1998) Investigation of the squeeze flow behaviour of sheet moulding compounds (SMC). Compos Part A 29(12):1569–1577
31. Le TH, Dumont PJJ, Orgéas L, Favier D, Salvo L, Boller E (2008) X-ray phase contrast microtomography for the analysis of the fibrous microstructure of SMC composites. Compos Part A 39:91–103
32. Le Corre S, Caillerie D, Orgéas L, Favier D (2004) Behavior of a net of fibers linked by viscous interactions: theory and mechanical properties. J Mech Phys Solids 52:395–421
33. Le Corre S, Dumont P, Orgéas L, Favier D (2005) Rheology of highly concentrated planar fiber suspensions. J Rheol 49:1029–1058
34. Le Corre S, Orgéas L, Favier D, Tourabi A, Maazouz A, Venet C (2002) Shear and compression behaviour of sheet molding compounds. Compos Sci Technol 62(4):571–577
35. Lee LJ, Marker LF, Griffith RM (1981) The rheology and mold flow of polyester sheet molding compound. Polym Compos 2(4):209–218
36. Lin C-M, Weng C-I, Ho C-T (1997) Anisotropy in sheet molding compounds during compression molding. Polym Compos 18(5):613–622
37. Lipscomb GG, Denn MM, Hur DU, Boger DV (1988) The flow of fiber suspensions in complex geometries. J Non-Newton Fluid Mech 26:297–325
38. Mackaplow MB, Shaqfeh ESG (1996) A numerical study of the rheological properties of suspensions of rigid, non-brownian fibres. J Fluid Mech 329:155–186
39. Meyssonier J, Duval P, Gagliardini O, Philip A (2001) Constitutive modelling and flow simulation of anisotropic polar ice, vol. Continuum mechanics and applications in geophysics and the environment. Springer, New York
40. Odenberger P, Andersson H, Lundström T (2004) Experimental flow-front visualisation in compression moulding of SMC. Compos Part A 35:1125–1134
41. Orgéas L, Dumont PJJ, Le TH, Favier D (2008) Lubricated compression of BMC, a concentrated and fibre reinforced granular polymer suspension. Rheol Acta 47:677–688
42. Osswald T, Tseng S-C (1994) Flow and rheology in polymer composites manufacturing, vol 10 of composites materials series. Elsevier, "Compression Molding", Ch 10. Elsevier, Amsterdam, pp 361–413
43. Phan-Thien N, Fan XJ, Tanner RI, Zheng R (2002) Folgar-tucker constant for a fibre suspension in a newtonian fluid. J Non-Newton Fluid Mech 103:251–260
44. Rabinovich M, Olsavsky K, Leach B, Cabrera-Rios M, Castro J (2008) Sheet molding compounds characterization using spiral flow. J Appl Polym Sci 109:2465–2471
45. Ranganathan S, Advani SG (1991) Fiber-fiber interactions in homogeneous flows of non-dilute suspensions. J Rheol 35:1499–1522
46. Sepehr M, Ausias G, Carreau PJ (2004) Rheological properties of short fiber filled polypropylene in transient shear flow. J Non-Newton Fluid Mech 123:19–32
47. Servais C, Luciani A, Månson J-A E (2002) Squeeze flow of concentrated long fibre suspensions: experiments and model. J Non-Newton Fluid Mech 104:165–184
48. Servais C, Månson J-A E, Toll S (1999) Fiber-fiber interaction in concentrated suspensions: disperse fibers. J Rheol 43(4):991–1004
49. Shaqfeh ESG, Fredrickson G (1990) The hydrodynamic stress in a suspension of rods. Phys Fluids 2(1):7–24
50. Silva-Nieto R, Fisher B (1981) Rheological characterization of unsatured polyester resin sheet molding compound. Polym Eng Sci 21(8):499–506
51. Souloumiac B, Vincent M (1998) Steady shear viscosity of short fibre suspensions in thermoplastics. Rheol Acta 37:289–298
52. Switzer LH, Klingenberg DJ (2003) Rheology of sheared flexible fiber suspensions via fiber-level simulations. J Rheol 47(3):759–778
53. Teyssier S, Bres S, Ohl B, Merle G (2003) Global analysis of orientation in BMC and relation with mechanical properties. In: SME (ed) Proc. Of ICCM-14. SME. San Diego, USA, pp 1–9
54. Thomasset J, Carreau P, Sanschagrin B, Ausias G (2005) Rheological properties of long glass fibre filled polypropylene. J Non-Newton Fluid Mech 125:25–34
55. Toll S (1998) Packing mechanics of fiber reinforcements. Polym Eng Sci 38:1337–1350
56. Toll S, Månson J-AE (1994) Dynamics of a planar concentrated suspension with non-hydrodynamic interaction. J Rheol 38(4):985–997
57. Vassal J-P (2007) Contribution à la modélisation des propriétés physiques et rhéologiques des milieux fibreux application à la mise en forme et aux propriétés thermiques des matériaux composites à fibres courtes. PhD thesis, Grenoble INP, France
58. Yamane Y, Kaneda Y, Doi M (1995) The effect of interaction of rodlike particles in semi-dilute suspensions under shear flow. J Phys Soc Jpn 64(9):3265–3274